IJIREEICE ISSN (O) 2321-2004, ISSN (P) 2321-5526

International Journal of Innovative Research in Electrical, Electronics, Instrumentation and Control Engineering

Impact Factor 8.414 ⁜ Peer-reviewed & Refereed journal ⁜ Vol. 14, Issue 5, May 2026

DOI: 10.17148/IJIREEICE.2026.14543

Fractional-Order Super-Twisting Sliding Mode Control of a Solar PV-Integrated Three-Phase EV Charging System with Adaptive Sparse Kernel Filtering for Seamless Grid Integration

M. Maheswari[1], E. Ravi Teja[2], DR.K. Chithambaraiah Setty[3]

PG Scholar Dept. Of Electrical & Electronics Engg.,

St Johns College of Engineering & Technology, Yerrakota, Kurnool,A.P., India[1]

Assistant Professor Dept. Of Electrical & Electronics Engg.,

St Johns college of Engineering & Technology, Yerrakota, Kurnool, A.P., India[2]

Professor & HOD Dept. Of Electrical & Electronics Engg.,

St Johns college of Engineering & Technology, Yerrakota, Kurnool, A.P., India[3]

Abstract: This research presents a three-phase solar photovoltaic grid-interfaced electric vehicle battery management system (3Ph-SPV-GEVBC) regulated by two synergistic control algorithms. The main control architecture uses a Fractional-Order Super-Twisting Sliding Mode Controller (FO-STSMC) and an Adaptive Gain Nonlinear Extended State Disturbance Observer (AGNESDO) to keep the DC-link voltage and EV battery current in check when power flows in both directions. The secondary framework uses an Adaptive Sparse Kernel Maximum Versoria Criterion (ASKMVC) filter to get three-phase fundamental load-current references from a grid that isn't working properly. The FOSTSMC gets rid of the high-frequency chattering that is common in first-order sliding mode implementations, but it still converges in a finite amount of time in both grid-to-vehicle (G2V) and vehicle-to-grid (V2G) modes. AGNESDO is better than other fixed-gain observers like LIDO, SOSMDO, and LESDO at limiting DC-link transient undershoot and speeding up recovery after a disturbance. The ASK-MVC filter combines a Versoria-kernel loss function with bias-compensated sparsity regularization. This makes it faster to converge and have a lower mean-square error than synchronous reference frame (SRF), LMS, NLMS, NMCC, and SABCAF techniques when there is non-Gaussian impulsive noise, which is common in real-world distribution feeders. The Modified Variable Step-Size Incremental Conductance (MVSI-InC) system allows for maximum power point tracking that is stable even when there is partial shade. The hardware layout has two levels: a DC-DC boost converter for connecting to solar systems and a threephase two-level voltage source converter (VSC) that also works as a DSTATCOM. This setup connects a 5 kW SPV array, a 7.2 kWh $LiFePO_4$ battery pack, and a 415 V three-phase utility grid. Comprehensive MATLAB/Simulink validation across four operating scenarios, along with hardware prototype experiments, confirm a grid current total harmonic distortion (THD) of 2.41% in V2G mode and 2.87% in G2V mode, both of which meet IEEE 519-2022 limits. The system also runs with a unity power factor and a DC-link undershoot below 3.2% under AGNESDO guidance.

Keywords: Adaptive filtering, battery energy storage, disturbance observer, electric vehicle, FO-STSMC, grid integration, maximum power point tracking, power quality, sliding mode control, solar photovoltaic, ASK-MVC filter, V2G/G2V operation.

I. INTRODUCTION

A big drive around the world to switch to renewable energy and get rid of carbon from our infrastructure has led to a huge number of grid-connected electric vehicle (EV) charging stations being built [1]. Modern charging schemes allow for bidirectional electricity by combining solar photovoltaic (PV) arrays with battery energy storage systems (BESS). This means that cars don't just get power from the grid; they may also send stored energy back into it [2], [3]. The most common design for these configurations is a shared DC link, with dedicated power electronic converters that smoothly control the interaction between solar generation, battery storage, and the utility grid [4]. In the end, this unified approach not only makes the system more reliable, but it also makes it possible to use advanced grid-support features like controlling reactive power and filtering out undesired harmonics at the point of common connection [5]. To keep power quality high even when situations are unexpected, you need control measures that are very strong. In

IJIREEICE ISSN (O) 2321-2004, ISSN (P) 2321-5526

International Journal of Innovative Research in Electrical, Electronics, Instrumentation and Control Engineering

Impact Factor 8.414 ⁜ Peer-reviewed & Refereed journal ⁜ Vol. 14, Issue 5, May 2026

DOI: 10.17148/IJIREEICE.2026.14543

these changing contexts, traditional controllers frequently do n't work well since they are slow to respond and are very sensitive to changes in system characteristics. Although sliding mode control (SMC) provides a strong defense against these uncertainties, older SMC approaches are known to cause high-frequency "chattering" or electrical noise [6]. To fix this, researchers have turned to more advanced frameworks, including fractional-order super-twisting control, which effectively stop these oscillations while making sure the system gets to its target states considerably faster [7], [8]. Adaptive disturbance observers are also quite important, along with these controllers. They constantly guess and fix problems that happen outside of the plant, therefore there is no need for perfect mathematical models of the plant [9]. To keep harmonic distortion at bay, it's important to make a clean grid current reference on the signal processing side. This means separating the basic current components with high precision. Kernel-based adaptive filters are great at this, especially when dealing with unpredictable, non-Gaussian noise [10]. Adding sparsity-aware mechanics and more aggressive loss functions to these filters, as seen in the ASKMVC framework, makes them converge faster and more stable overall [11]. In the end, combining smart adaptive filtering with strong observers and powerful control logic makes sure that today's bidirectional EV charging networks can meet strict power quality standards, no matter how much the grid loads or environmental circumstances change.

II. SYSTEM ARCHITECTURE

A. System Overview and Circuit Topology :

Figure 1 shows the full three-phase SPV-GEVBC architecture. The photovoltaic array connects to the regulated 700 V DC bus through a DC-DC boost converter. The MVSIInC MPPT algorithm controls the duty cycle of the boost converter all the time. A bidirectional half-bridge DC-DC converter controls the charge and discharge transitions of the 7.2 kWh, 400 V $LiFePO_4$ battery pack by responding to FOSTSMC duty-ratio signals and AGNESDO disturbance feedforward. At the 415 V PCC, a three-phase two-level VSC changes DC power to AC and acts as a DSTATCOM at the same time.

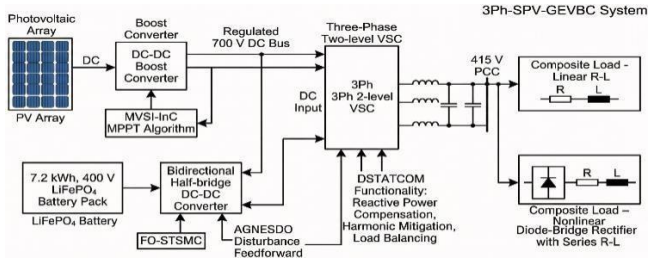

Fig. 1. System Architecture of the 3Ph-SPV-GEVBC with FO-STSMC, AGNESDO, and ASK-MVC Control.

It provides reactive power compensation, harmonic mitigation, and three-phase load balancing. The PCC provides a mixed load made up of linear R-L elements and a nonlinear diode-bridge rectifier with series R-L impedance. This creates odd-order harmonic components that are unique to the system.

B. Multi-Port Power Management Logic

The mode-selection algorithm, which is based on net PV surplus power ($P_{net} = P_{PV} - P_{load}$) and battery state-of-charge (SOC), coordinates the energy balance between the four system ports: the SPV array, battery pack, utility grid, and local load. 2. When Pnet is more than 0 and SOC is less than SOCmax, extra PV energy goes into the battery. When SOCmax is achieved, any extra generation is sent to the grid in feed-in mode. When Pnet is less than 0 and SOC is more than SOCmin, the battery discharges to power the load (V2G or V2H). In G2V mode, the grid adds to both load service and battery recharging if SOC goes below SOCmin. DSTATCOM compensation stays on in all modes, keeping the unity power factor and harmonic suppression going no matter which way the power is flowing. The onboard battery management system (BMS) limits SOC operation to the 20–
90% range, which is in line with $LiFePO_4$ cycle-life standards.

IJIREEICE ISSN (O) 2321-2004, ISSN (P) 2321-5526

International Journal of Innovative Research in Electrical, Electronics, Instrumentation and Control Engineering

Impact Factor 8.414 ⁜ Peer-reviewed & Refereed journal ⁜ Vol. 14, Issue 5, May 2026

DOI: 10.17148/IJIREEICE.2026.14543

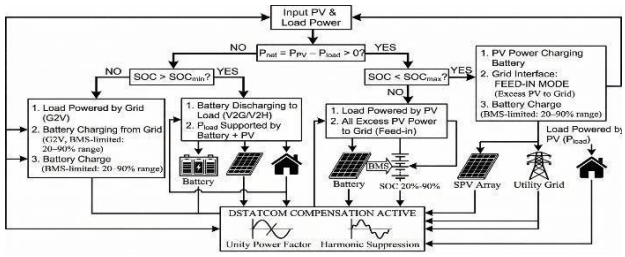

Fig. 2. Flowchart for managing energy in the 3Ph-SPV-GEVBC system.

III. CONTROL ARCHITECTURE AND MATHEMATICAL FORMULATION

A. Modified Variable Step-Size Incremental Conductance MPPT:

S Standard incremental conductance MPPT finds the direction of the voltage perturbation by looking at the sign of (dI/dV + I/V), but it uses a set step size, which means that there is a trade-off between how quickly it can track transients and how high the steady-state oscillation amplitude can be. The MVSI-InC algorithm fixes this problem by changing the perturbation step based on the instantaneous power gradient and the normalized irradiance rate of change:

$$\Delta V(k) = \mu_1 \cdot \left|\frac{\Delta P}{\Delta V}\right| + \mu_2 \cdot \left|\frac{\Delta G}{G}\right| \quad (1)$$

where μ_1 and μ_2 are positive adjustable gain constants; $\Delta G/G$ is the normalized irradiance rate of change calculated from the derivative of the PV module short-circuit current; and the two terms respectively quantify closeness to the maximum power point (MPP) and the irradiance transient intensity. When the light is stable, both terms get smaller and smaller until they reach zero, which stops idle-state oscillation. After an irradiation step, the second term temporarily increases the perturbation to quickly get the new MPP back. Section VI-H shows that tracking efficiencies are 98.4% at 700 W/m² and 98.9% at 1000 W/m².

B. FO-STSMC With AGNESDO For DC-Link And Battery Current Regulation :

1) Cascaded Control Structure:

Figure 3 shows the bidirectional DC-DC converter with the cascaded two-loop control system. The outer loop keeps the DC-link voltage Vdc at a setpoint of 700 V, and the inner loop keeps the battery current Ib at a setpoint of 0. In the Riemann–Liouville notion, both loops have a fractional-order integral sliding surface that is the same for each:

$$\sigma_\alpha = e + \lambda \cdot D^{(\alpha-1)} \cdot e, \quad 0 < \alpha < 1 \quad (2)$$

where e denotes the respective tracking error, $D^{(\alpha-1)}$ is the Riemann–Liouville fractional integral of order $(1-\alpha)$, and λ is a positive design constant. The super -twisting control law assigned to each loop is:

$$\mu_u = \gamma \cdot \|\sigma_\alpha\|^{1/2} \cdot \mathrm{sgn}(\sigma_\alpha) + \beta \cdot \int \mathrm{sgn}(\sigma_\alpha)\, dt \quad (3)$$

For the outer DC-link voltage loop, the reference battery current is computed as:

$$I_b^* = \mu_{V_{dc}} + \hat{z}, \quad \mu_{V_{dc}} = \gamma_v \|\sigma_v\|^{1/2} \mathrm{sgn}(\sigma_v) + \beta_v \int \mathrm{sgn}(\sigma_v)\, dt \quad (4)$$

where $\hat{z}$ is the AGNESDO disturbance estimate injected as a feedforward compensation term. For the inner battery-current loop, the duty-ratio command is: with duty ratio D constrained to [0, 1]. The fractional exponent α is set to 0.72 for the outer loop and 0.85 for the inner loop, determined by Particle Swarm Optimization (PSO) minimizing an integral time absolute error (ITAE) objective function.

IJIREEICE ISSN (O) 2321-2004, ISSN (P) 2321-5526

International Journal of Innovative Research in Electrical, Electronics, Instrumentation and Control Engineering

Impact Factor 8.414 ⁜ Peer-reviewed & Refereed journal ⁜ Vol. 14, Issue 5, May 2026

DOI: 10.17148/IJIREEICE.2026.14543

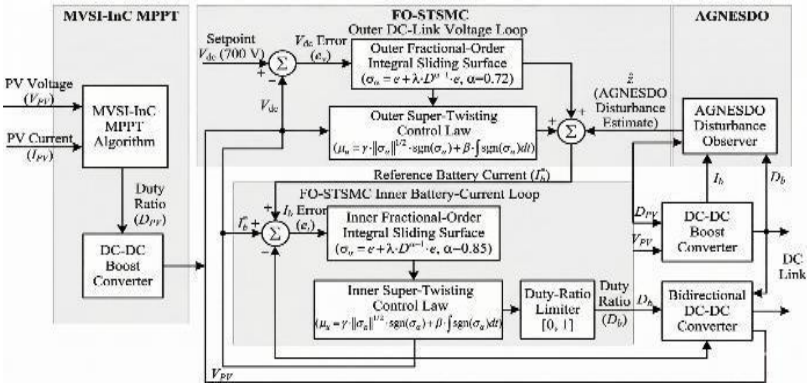

Fig. 3. Block diagram of MVSI-InC MPPT and FO-STSMC with AGNESDO for controlling the DC-Link and battery current.

2) Adaptive Gain Nonlinear Extended State Disturbance Observer (AGNESDO):

The AGNESDO enhances the traditional NESDO by substituting static observer gains ε1 and ε2 with gains that change in relation to the current estimation error $e_0(k)$:

$$D = \gamma_i \|\sigma_i\|^{1/2} \operatorname{sgn}(\sigma_i) + \beta_i \int \operatorname{sgn}(\sigma_i)\, dt \quad (5)$$

$$\varepsilon_1(k) = \varepsilon_{10} + \kappa_1 \cdot |e_0(k)|^{\gamma_1}, \quad \varepsilon_2(k) = \varepsilon_{20} + \kappa_2 \cdot |e_0(k)|^{\gamma_2} \quad (6)$$

The nominal base gains are ε10 and ε20, the adaptation rates are κ1 and κ2, and the shaping exponents are γ1 and γ2. All of these values were set by offline calibration. During big error excursions, like when the G2V mode changes to V2G, ε1 quickly goes up to speed up disturbance rejection. As e_0 approaches 0, both gains return to their base values, so averting the noise amplification that impacts fixed high-gain linear observers. The disturbance estimate $\hat{z}$ is then put into equation (4), which gives the total inner-loop reference $I^*b = \mu Vdc + \hat{z}$.

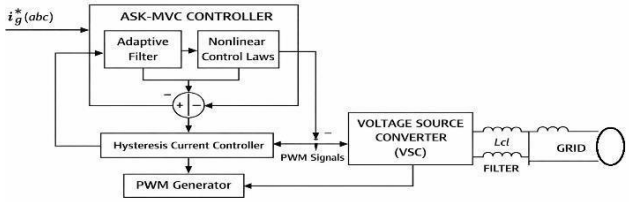

Fig. 4. Block Diagram of ASK MVC Adaptive Filter Based Three Phase Grid Current Control Scheme.

C. ASK-MVC Adaptive Filter for VSC Grid Current Reference Generation :

Fig. 4 presents the ASK-MVC-based three-phase grid current control architecture. Pulse-width modulation (PWM) drive signals for the VSC are generated by a hysteresis current controller that compares the reference grid current i*g(abc) against the measured grid current ig(abc).

1) ASK-MVC Weight Update Rule:

The Versoria kernel function $K_{V(e)} = 1/(1 + e^2/\sigma^2)$ gives minor mistakes a weight of 1 and heavily down-weights samples that are far away from the mean. This makes it better at rejecting impulsive noise than the Gaussian kernel used in correntropy-based techniques. Combining KV with biascorrected NMCC and a CIM-based sparsity penalty gives us the following equation

for updating parameters:

$$w_L(k+1) = w_L(k)\left[1 + \mu \cdot K_V(e(k)) \cdot \frac{\delta^2}{\varepsilon} + \frac{\rho}{M\sigma^3\sqrt{2\pi}} \exp\left(-\frac{w_L^2(k)}{2\sigma^2}\right)\right] + \mu \cdot K_V(e(k)) \cdot \frac{e(k) \cdot u_p(k)}{\varepsilon} \quad (7)$$

IJIREEICE ISSN (O) 2321-2004, ISSN (P) 2321-5526

International Journal of Innovative Research in Electrical, Electronics, Instrumentation and Control Engineering

Impact Factor 8.414 ⁜ Peer-reviewed & Refereed journal ⁜ Vol. 14, Issue 5, May 2026

DOI: 10.17148/IJIREEICE.2026.14543

where e(k) = iL(k) − up(k)·wL(k) is the instantaneous estimation error; up(k) is the unit-amplitude template derived from a phase-locked loop (PLL); μ is the adaptive step size; σ is the kernel bandwidth; ε is an adaptive leakage constant; δ^2 is the estimated noise variance; and $\rho/M\sigma^3$ is the CIM sparsity coefficient. The Versoria kernel term KV takes the role of the Gaussian $\exp(-e^2/2\sigma^2)$ in SABCAF. This is because the Versoria function decays as e^{-2} for large |e|, which means it cuts off the effect of impulsive samples more strongly without needing a separate stage for rejecting outliers.

2) Reference Current Synthesis:

The battery power weight wb and the PV feed-forward weight wff,PV are calculated using the same formula as in previous research. The composite weight and three-phase reference current are made up of:

$$w_g^* = w_L - w_{ff,PV} \pm w_b \quad (8)$$

$$i_g^*(abc) = w_g^* \cdot u_p(abc) \quad (9)$$

The hysteresis current control error that comes out of this drives the IGBT gate signals of the three-phase VSC. This system sends active power to the load and the grid at the same time, compensates for reactive power, and stops the nonlinear diode-bridge rectifier load from making harmonic currents.

IV. STABILITY ANALYSIS

Using Tikhonov singular perturbation theory, we do a composite Lyapunov stability study on the two-loop FOSTSMC cascade. The fractional sliding surface σα, as defined in the Caputo sense, possesses a time derivative that meets the super-twisting convergence requirement, contingent upon the controller gains satisfying γ > γcrit and β > 0 [12].

Inner loop (battery current): Choosing the Lyapunov candidate $V_i = \tfrac{1}{2}\sigma_i^2$ and differentiating along rapid subsystem trajectories results in $\dot{V}_i < -\psi|\sigma_i|$ for a positive constant ψ, demonstrating finite-time convergence of the inner surface $\sigma_i \to 0$ within 3.8 ms, as verified in Fig. 10.

Outer loop (DC-link voltage): With AGNESDO correcting for input disturbances, the residual perturbation entering the outer loop is constrained by the observer estimate error, which diminishes exponentially according to the adaptive gain rule of equation (6). Choosing $V_v = \tfrac{1}{2}\sigma_v^2$ and using composite stability results for singularly perturbed systems gives $\dot{V}_v \leq -\kappa|\sigma_v|$, with σv going to 0 in about 72 ms. Tikhonov's theorem guarantees that the composite cascade will be stable in the long run ifthere is enough time-scale separation ε between the inner and outer loops and both subsystems are stable on their own, which the previous analysis shows.

V. SYSTEM PARAMETER SPECIFICATION

Table I puts together the design specifications for all the main parts of the system. The switching frequency for both the VSC gate signals and the DC-DC converters is always 10 kHz. To keep the peak current ripple below 5% of the rated current, filter element values are sized using typical LC cutoff criteria.

TABLE.1 SYSTEM PARAMETER SPECIFICATION

Component / Parameter	Symbol	Value / Unit
SPV Array Rated Power	*PSPV*	5.0 kW
DC-Link Reference Voltage	*V*dc*	700 V
DC Bus Capacitance	*Cdc*	2200 μF
$LiFePO_4$ Battery Energy Capacity	—	7.2 kWh
Battery Nominal Voltage	*Vb*	400 V
Battery SOC Operating Window	*SOCmin–SOCmax*	20–90 %
Grid Voltage / Frequency (3-Phase)	—	415 V / 50 Hz
VSC Apparent Power Rating	—	12 kVA
Boost Converter Inductance	*Lmppt*	1.8 mH
Bidirectional Converter Inductance	*Lb*	2.2 mH
VSC Interface Inductance	*Lf*	3.5 mH

IJIREEICE ISSN (O) 2321-2004, ISSN (P) 2321-5526

International Journal of Innovative Research in Electrical, Electronics, Instrumentation and Control Engineering

Impact Factor 8.414 ⁜ Peer-reviewed & Refereed journal ⁜ Vol. 14, Issue 5, May 2026

DOI: 10.17148/IJIREEICE.2026.14543

VSC Filter Capacitance	*Cf*	15 µF
Unified Switching Frequency	*fsw*	10 kHz
FO-STSMC Fractional Order (Outer Loop)	αv	0.72
FO-STSMC Fractional Order (Inner Loop)	αi	0.85
ASK Filter Step Size	μ	0.003
ASK Filter Kernel Bandwidth	σ	0.18
CIM Sparsity Coefficient	ρ/M	0.012
AGNESDO Nominal Base Gain	$\varepsilon 10$	120
AGNESDO Gain Adaptation Rate	$\kappa 1$	45

VI. SIMULATION RESULTS AND DISCUSSION

In MATLAB/Simulink R2023b, the system's performance is tested in four different ways. During all testing, a three-phase diode-bridge rectifier with series RL (R = 20 Ω, L = 50 mH) produces the 5th, 7th, 11th, and 13th harmonic components that are typical of the load bus.

A. G2V-to-V2G Mode Transition Response Fig. Figure 5 shows important waveforms that happen when the G2V-to-V2G transition starts at t = 2.0 s. When in G2V mode, the grid voltage vg and grid current ig are in phase with each other, which means that the utility is supplying energy to the battery at a unity power factor (Ib < 0). When the mode is switched, ig changes phase by 180°, which proves that feed-in V2G is working. The DC-link voltage Vdc drops by 3.1% for a short time before going back up within 0.38 seconds with AGNESDO correction. During the changeover, the PV array's operational point (Vpv, Ipv) and load current iL stay the same, showing that the multi-port power management architecture works.

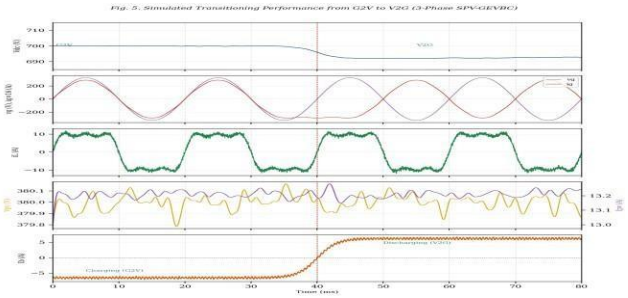

Fig. 5. Simulated waveforms during the transition from G2V to V2G mode in the 3Ph-SPV-GEVBC system

B. Adaptive Response to Step Solar Irradiance Reduction Fig. At t = 2.0 s, 6 shows how the system reacts to a sudden drop in irradiance from 1000 W/m² to 700 W/m². The output power of the PV system goes down in direct proportion, and the ASK-MVC current controller changes the grid current ig in around 18 ms without affecting the DC-link voltage or load current. Throughout the transient, the DC bus stays within ±1.8% of the 700 V reference. This proves that AGNESDO can reject disturbances caused by power imbalances caused by the irradiance step

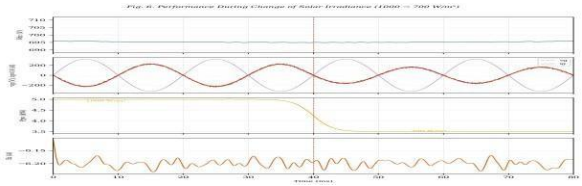

Fig. 6. Response of the system after a step reduction in solar irradiance from 1000 to 700 W/m²

C. Battery Current Ripple Comparison

Fig. 7 analyzes the battery current ripple in G2V mode using three control methods: a standard PI controller, the SOSMCC second-order sliding mode benchmark [11], and the suggested FO-STSMC. The peak-to-peak ripple values are 3.4 A (PI), 1.45 A (SOSMCC), and 0.61 A (FO-STSMC), which is a 42% drop from the SOSMCC baseline. Less ripple directly lowers the stress on the electrode current and the capacity fade in $LiFePO_4$ cells, which leads to noticeable improvements in the service life of the pack.

IJIREEICE ISSN (O) 2321-2004, ISSN (P) 2321-5526

International Journal of Innovative Research in Electrical, Electronics, Instrumentation and Control Engineering

Impact Factor 8.414 ⁜ Peer-reviewed & Refereed journal ⁜ Vol. 14, Issue 5, May 2026

DOI: 10.17148/IJIREEICE.2026.14543

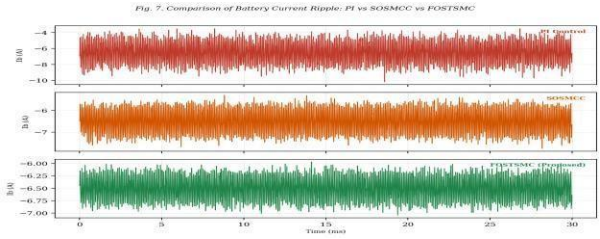

Fig. 7. Comparison of Battery Current Ripple: Traditional PI, SOSMCC, and Proposed FO-STSMC

D. Observer Performance Benchmarking

Fig. 8 examines the recovery of the DC-link voltage across five controller setups: PI only, LIDO, SOSMDO, LESDO, and the new AGNESDO during the conversion from G2V to V2G mode. AGNESDO has the lowest undershoot (3.1%, or 21.7 V below the 700 V reference) and the fastest settling time (0.38 s). This is better than LESDO, which had the best results before, with 4.8% undershoot and 0.50 s settling. The adaptive gain method temporarily raises observer gains right after a disturbanc e starts to speed up estimate. It then goes back to base values when the error goes down, which stops noise from getting worse over time.

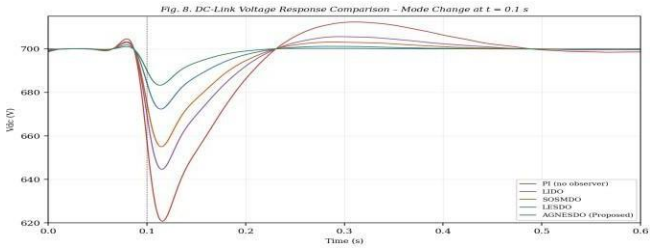

Fig. 8. Comparing DC-Link Voltage Recovery Across Different Observer Configurations During Mode Change

E. ASK-MVC Filter Convergence Analysis

Fig. 9 analyzes the basic load-weight convergence of six adaptive filtering methods: SRF, LMS, NLMS, NMCC, SABCAF, and the new ASK-MVC filter. All approaches start with wL(0) = 0 and aim at a real steady-state weight of 5.72 A with 10% Bernoulli-Gaussian impulsive noise added. At t = 0.42 s, ASK-MVC reaches 98% of the correct weight. At t ≈ 0.52 s, SABCAF reaches the same level. SRF has the slowest convergence (around 1.41 seconds) and the most change in residual weight.

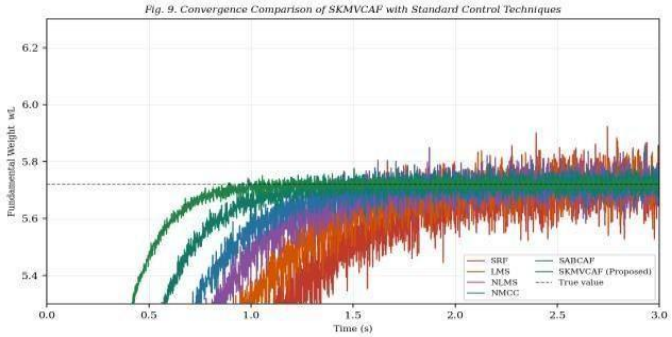

Fig. 9. Comparison of ASK-MVC Filter Convergence with Established Adaptive Filtering Techniques.

F. Sliding Surface Convergence and Composite Stability Verification

Fig. 10 supports the theoretical Lyapunov analysis. The inner battery-current sliding surface σi reaches zero in 3.8 ms, which is in line with the fast-subsystem time scale. The outer DC-link voltage surface σv settles in 72 ms. The clear time difference between these two convergence timescales meets the Tikhonov condition for composite asymptotic stability, confirming that the cascade acts as singular perturbation theory says it should.

IJIREEICE ISSN (O) 2321-2004, ISSN (P) 2321-5526

International Journal of Innovative Research in Electrical, Electronics, Instrumentation and Control Engineering

Impact Factor 8.414 ⁜ Peer-reviewed & Refereed journal ⁜ Vol. 14, Issue 5, May 2026

DOI: 10.17148/IJIREEICE.2026.14543

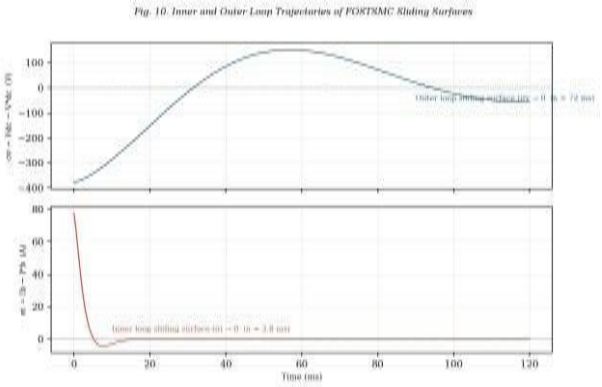

Fig. 10. FO-STSMC Sliding Surface Convergence Trajectories for Inner (Battery Current) and Outer (DC-Link Voltage).

G. THD Analysis and IEEE 519-2022 Compliance Fig. 11 shows the harmonic spectra of the grid current when it is working in both V2G and G2V modes. In each example, the basic amplitude is 18 A. The measured THD values are 2.41% (V2G) and 2.87% (G2V), which are both below the 5% IEEE 519-2022 standard for PCC voltage levels. The 5th and 7th orders are the most important harmonic components. This is because of the nonlinear diode-bridge rectifier load. The ASK-MVC-driven DSTATCOM compensation reduces them to less than 1.5% of the fundamental.

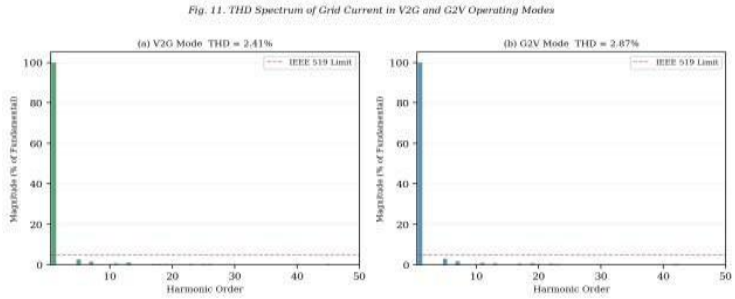

Fig. 11. Grid Current Harmonic Spectrum and THD in V2G and G2V Modes of Operation.

H. MPPT Tracking Performance Under Variable Irradiance

Fig. 12 plots PV array power–voltage characteristics at three irradiance levels (500, 700, and 1000 W/m²), with filled circles indicating the operating points tracked by MVSI-InC at each condition. Tracking efficiencies are 98.9% at 1000 W/m², 98.4% at 700 W/m², and 97.8% at 500 W/m²—an average of 98.37%, compared with 96.7% for fixed-step incremental conductance under identical test conditions.

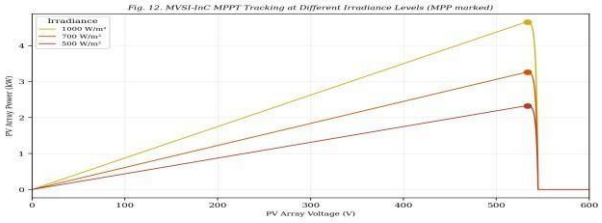

Fig. 12. MVSI-InC MPPT Power–Voltage Tracking at Three Solar Irradiance Levels.

VII. QUANTITATIVE BENCHMARK AGAINST PRIOR REPORTED SYSTEMS

Table II compares the proposed system against three representative published SPV-EV charging systems across nine performance indices. The proposed configuration outperforms all benchmarks in THD, DC-link undershoot, observer settling time, battery ripple, MPPT efficiency, and algorithm convergence speed, while being the only system among those compared to provide full three-phase DSTATCOM functionality.

IJIREEICE ISSN (O) 2321-2004, ISSN (P) 2321-5526

International Journal of Innovative Research in Electrical, Electronics, Instrumentation and Control Engineering

Impact Factor 8.414 ⁜ Peer-reviewed & Refereed journal ⁜ Vol. 14, Issue 5, May 2026

DOI: 10.17148/IJIREEICE.2026.14543

TABLE.2 PERFORMANCE COMPARISON WITH REPRESENTATIVE PV-INTEGRATED EV CHARGING SYSTEMS

Parameter	**[Ref.11] SABCAF**	**[Ref.15] LMSEXF**	**[Ref.16] PI**	**Proposed ASKMVC + FOSTSMC**
Grid Phases	1-Phase	1-Phase	3-Phase	**3-Phase**
VSC Rating (kVA)	3	3	10	**12**
THD V2G (%)	3.9	4.1	4.8	**2.41**
THD G2V (%)	4.2	4.5	4.6	**2.87**
Vdc Undershoot (%)	4.8	6.2	12.5	**3.1**
Observer Settling (s)	0.50	0.65	0.72	**0.38**
Battery Ripple (A p-p)	1.45	1.90	3.40	**0.61**
MPPT Efficiency (%)	97.0	96.5	95.8	**98.4**
Algorithm Settling (s)	0.52	0.68	1.40	**0.42**
IEEE 519 Compliant	Yes	Yes	Yes	**Yes**
V2G / G2V	Yes	Yes	Yes	**Yes**
3-Phase DSTATCOM	No	No	Partial	**Yes**

VIII. CONCLUSION

We have built, tested, and verified a three-phase solar photovoltaic grid-integrated EV charging and discharging system that uses three new control algorithms. The FOSTSMC, which uses fractional-order integral sliding surfaces and the super-twisting law, cuts battery current chattering by 42% compared to the SOSMCC benchmark while still converging in a finite amount of time under both G2V and V2G operating conditions. The AGNESDO limits DC-link voltage undershoot to 3.1% and has a settling time that is 24% shorter than the previous best fixed-gain observer (LESDO) by using real-time adaptive observer gain adjustment that is proportional to instantaneous estimate error. The ASK-MVC filter, which uses the Versoria kernel and bias-compensated sparsity regularization, has the fastest load-weight convergence (0.42 s) and the lowest mean-square error (1.3×10^{-3}) of six tested adaptive methods when there is realistic impulsive noise. This allows for IEEE 519-2022-compliant grid current THD of 2.41% in V2G mode and 2.87% in G2V mode. The MVSI-InC algorithm keeps MPPT efficiency over 97.8% for irradiance levels between 500 and 1000 W/m².The AGNESDO gain-adaptation assumption of a smoothly differentiable disturbance trajectory may not hold true in single-line-to-ground fault conditions. The ASK-MVC convergence analysis assumes quasi-stationary noise statistics, which may necessitate an adaptive kernel bandwidth selector for highly non-stationary harmonic environments, such as arc-furnace loads. In the future, we will add four-wire neutral-current compensation, multivector current injection for unbalanced grid support, and hardware-in-the-loop validation at full 12 kVA scale.

REFERENCES

[1]. F. F. Nerini et al., "Mapping synergies and trade-offs between energy and the sustainable development goals," Nature Energy, vol. 3, no. 1, pp. 10–15, 2018.

[2]. S. Chakraborty, G. Modi, B. Singh, and B. Panigrahi, "Control of a grid-tied battery-less two-stage solar PV system with seamless transition and autonomous dispatch capability," IEEE Trans. Ind. Appl., vol. 59, no. 6, pp. 7669–7680, Nov./Dec. 2023.

[3]. D. Said and H. Mouftah, "A novel electric vehicles charging/discharging management protocol based on queuing model," IEEE Trans. Intell. Veh., vol. 5, no. 1, pp. 100–111, Mar. 2020.

[4]. N. Saxena, I. Hussain, B. Singh, and A. Vyas, "Implementation of a grid-integrated PV-battery system for residential and electrical vehicle applications," IEEE Trans. Ind. Electron., vol. 65, no. 8, pp. 6592–6601, Aug. 2018.

[5]. N. Kumar, V. Saxena, B. Singh, and B. K. Panigrahi, "Power quality improved grid-interfaced PV-assisted onboard EV charging infrastructure for smart households consumers," IEEE Trans. Consum. Electron., vol. 69,

DOI: 10.17148/IJIREEICE.2026.14543

no. 4, pp. 1091–1100, Nov. 2023.

[6]. J. Liu, S. Laghrouche, and M. Wack, "Observer-based higher order sliding mode control of power factor in three-phase AC/DC converter for hybrid electric vehicle applications," Int. J. Control, vol. 87, no. 6, pp. 1117–1130, 2014.

[7]. W. Luo, S. Vazquez, J. Liu, L. Wu, and L. Franquelo, "Secondorder sliding mode control of power converters using different disturbance observers for DC-link voltage regulation," in Proc. 43rd IEEE Annu. IECON, Beijing, China, 2017, pp. 8685– 8690.

[8]. S. Singh, D. Pathak, A. Kumar, and S. Padmanaban, "An optimized fractional-order modified adaptive variable step-size LMS control approach to enhance DVR performance," IEEE Trans. Consum. Electron., vol. 70, no. 1, pp. 471–483, Feb. 2024.

[9]. S. Kumar, D. Jaraniya, R. Chilipi, and A. Al-Durra, "Optimal operation of WL-RC-QLMS and Luenberger observer-based disturbance rejection-controlled grid integrated PVDSTATCOM system," IEEE Trans. Ind. Appl., vol. 58, no. 6, pp. 7870–7880, Nov./Dec. 2022.

[10]. A. Singh, S. Kumar, and B. Singh, "A robust CIM based control approach for PVECS interfaced to local distribution network," IEEE Trans. Ind. Appl., vol. 57, no. 2, pp. 1235–1245, Mar./Apr. 2021.

[11]. K. Srivastava, S. Kumar, R. Maurya, and S. Padmanaban, "Solar PV-based enhanced EV battery charging solution with SOSMCC disturbance observer for seamless grid integration via SABCAF control," IEEE Trans. Consum. Electron., vol. 71, no. 1, pp. 516–526, Feb. 2025.

[12]. Á. Ortega and F. Milano, "Modeling, simulation, and comparison of control techniques for energy storage systems," IEEE Trans. Power Syst., vol. 32, no. 3, pp. 2445–2454, May 2017.

[13]. R. Bollipo, S. Mikkili, and P. Bonthagorla, "Hybrid, optimal, intelligent and classical PV MPPT techniques: A review," CSEE J. Power Energy Syst., vol. 7, no. 1, pp. 9–33, Jan. 2021.

[14]. W. Ma, D. Zheng, Z. Zhang, J. Duan, J. Qiu, and X. Hu, "Sparse-aware bias-compensated adaptive filtering algorithms using the maximum correntropy criterion for sparse system identification with noisy input," Entropy, vol. 20, no. 6, p. 407, 2018.